

UCLA

UCLA Previously Published Works

Title

Atomic view of an amyloid dodecamer exhibiting selective cellular toxic vulnerability in acute brain slices

Permalink

<https://escholarship.org/uc/item/2jx5j3d7>

Journal

Protein Science, 31(3)

ISSN

0961-8368

Authors

Gray, Amber LH
Sawaya, Michael R
Acharyya, Debalina
[et al.](#)

Publication Date


2022-03-01

DOI

10.1002/pro.4268

Peer reviewed

Atomic view of an amyloid dodecamer exhibiting selective cellular toxic vulnerability in acute brain slices

Amber L. H. Gray¹ | Michael R. Sawaya^{2,3,4,5,6} | Debalina Acharyya⁷ |
 Jinchao Lou¹ | Emery M. Edington¹ | Michael D. Best¹ | Rebecca A. Prosser⁷ |
 David S. Eisenberg^{2,3,4,5,6} | Thanh D. Do¹ 

¹Department of Chemistry, University of Tennessee, Knoxville, Tennessee, USA

²HHMI, University of California, Los Angeles, California, USA

³Department of Chemistry and Biochemistry, University of California, Los Angeles, California, USA

⁴Department of Biological Chemistry, University of California, Los Angeles, California, USA

⁵Molecular Biology Institute, University of California, Los Angeles, California, USA

⁶Department of Energy Institute for Genomics and Proteomics, University of California, Los Angeles, California, USA

⁷Department of Biochemistry & Cellular and Molecular Biology, University of Tennessee, Knoxville, Tennessee, USA

Correspondence

Thanh D. Do, Department of Chemistry
 University of Tennessee, Knoxville 1420
 Circle Drive Buehler 616 Knoxville, TN
 37996, USA.
 Email: tdo5@utk.edu

Funding information

Thanh D. Do gratefully acknowledges the laboratory start-up from the University of Tennessee and Department of Chemistry, the global academic support program from Agilent, and the startup allocation (MCB200047) from the Extreme Science and Engineering Discovery Environment (XSEDE), which is supported by National Science Foundation grant number ACI-1548562. Amber L. H. Gray was partially supported by the Eastman Summer Fellowship. Michael D. Best acknowledges the support from NSF DMR-1807689. The X-ray crystallographic experiments were conducted at the Northeastern Collaborative Access Team beamlines, which are funded by the National Institute of General Medical Sciences from the National Institutes of Health (P30 GM124165). This research used resources of the Advanced Photon Source, a U.S. Department of Energy (DOE) Office

Abstract

Atomic structures of amyloid oligomers that capture the neurodegenerative disease pathology are essential to understand disease-state causes and finding cures. Here we investigate the G6W mutation of the cytotoxic, hexameric amyloid model KV11. The mutation results into an asymmetric dodecamer composed of a pair of 30° twisted antiparallel β -sheets. The complete break between adjacent β -strands is unprecedented among amyloid fibril crystal structures and supports that our structure is an oligomer. The poor shape complementarity between mated sheets reveals an interior channel for binding lipids, suggesting that the toxicity may be due to a perturbation of lipid transport rather than a direct disruption of membrane integrity. Viability assays on mouse suprachiasmatic nucleus, anterior hypothalamus, and cerebral cortex demonstrated selective regional vulnerability consistent with Alzheimer's disease. Neuropeptides released from the brain slices may provide clues to how G6W initiates cellular injury.

KEYWORDS

amyloid oligomers, brain slices, ion-mobility mass spectrometry, suprachiasmatic nucleus, X-ray crystallography

Abbreviations: AD, Alzheimer's disease; AH, anterior hypothalamus; DAPI, 4',6-diamidino-2-phenylindole; IMS-MS, ion mobility spectrometry-mass spectrometry; LC, liquid chromatography; PI, propidium iodide; SCN, suprachiasmatic nucleus.

Amber L. H. Gray and Michael R. Sawaya contributed equally to this study.

of Science User Facility operated for the DOE Office of Science by Argonne National Laboratory under Contract No. DE-AC02-06CH11357.

1 | INTRODUCTION

Transient oligomeric species formed during protein misfolding and aggregation have been implicated as the toxic agent for many neurodegenerative diseases, including Alzheimer's disease (AD),^{1,2} Huntington's disease,³ Parkinson's disease,⁴ and amyotrophic lateral sclerosis (ALS).⁵ Conformational heterogeneity and co-aggregation of several proteins, such as the plaques of amyloid- β (A β) and tangles of hyperphosphorylated tau observed in AD,⁶ contribute to the complex etiology of the diseases. Further compounding the complexity of these diseases is the aspect of selective cellular/regional vulnerability, where deposits of protein aggregates are more prominent in specific regions of the brain and cause more damage to certain types of cells but not others.⁷ For example, slow-firing motor neurons are more resilient than their fast-fatigable counterparts in ALS pathology.^{8–11} Thus, cellular heterogeneity, even among similar cell types,⁹ must also be taken into account when investigating such diseases. Understanding how certain cell types in some brain regions are able to resist amyloid toxicity is essential to developing novel therapeutic strategies.

Efforts to replicate how toxic oligomers initiate and propagate disease conditions have enlisted the use of cellular mimetics^{12,13} or relied on the outcomes of (colorimetric) cell viability assays.^{5,14,15} However, the latter is often hypothesis-centric and performed on commercial cell lines, which do not account for cellular heterogeneity and inter-cellular communication. Acute tissue slices provide an alternative to commercial cell lines where different brain regions containing multiple cell types can be evaluated while maintaining in vivo tissue structure. Identifying cell types that are resilient to amyloid toxicity may elucidate endogenous molecules that provide protection against the disease toxins. Moreover, to clarify how small but toxic amyloid oligomers affect brain tissues, amyloid models with known structures should be investigated. As we will demonstrate in this article, an attempt to disrupt one type of toxic oligomer may lead to the formation of different, larger, more structurally complex, and toxic oligomers. The multifaceted research path outlined here has not been fully exploited in AD research.

In this study, we started with the 11-residue segment of the α B-crystallin protein (KVKVLGDVIEV), referred to here as KV11, previously shown by the Eisenberg group to form cylindrical hexamers (termed cylindrins).¹⁴ Several 11-residue peptides from A β ¹⁶ and TAR DNA-

binding protein of 43 kDa (TDP-43) were proposed to form similar structural motifs.^{16,17} It was hypothesized that depending on the length and amino acid composition of the peptide, either cylindrin or a β -barrel could be formed. For example, Do et al. showed by IMS-MS and molecular dynamics simulation that A β (25–35) forms an octameric β -barrel.¹⁶

Because the glycine in the sixth position is essential to the structural integrity of toxic amyloid-like cylindrin assemblies,^{5,14} it is logical to predict that a mutation of glycine to a bulky residue, such as tryptophan, would prevent cylindrin formation and alleviate cytotoxicity. Here, we will show that the opposite is true; as one type of toxic amyloid structures is disrupted, another type that is more toxic can be introduced. Experiments to identify and separate transient oligomers of KV11 and KV11^{G6W} (hereafter referred to as G6W) reveal different species formed from these two distinct peptide species. Ion mobility spectrometry–mass spectrometry (IMS–MS) has been used previously for similar tasks.^{5,16} In IMS–MS, isobaric oligomers with the same *mass-to-charge* ratio (*m/z*) can be separated by measuring their drift times. We complement the IMS–MS work with X-ray crystallography to unambiguously determine some of the structure states of G6W. To gain insight into how these structures influence biochemistry, we investigated how KV11 and G6W interact with healthy brain tissue. Specifically, we explored how G6W and KV11 differentially affect cells within distinct brain regions using viability assays with propidium iodide (PI). Using liquid chromatography (LC)-IMS–MS, we interrogated subtle changes in the peptides released from mouse brain slices incubated with G6W. Finally, ligand binding pockets discovered in our structure of G6W led us to investigate the effect of membrane mimetics on oligomerization and stability of G6W oligomers.

2 | RESULTS AND DISCUSSION

2.1 | Mouse brain slices exhibit selective regional vulnerability to KV11 and G6W

We investigated the relative toxicity of KV11 and G6W across three brain regions. KV11 has previously been shown to exhibit cytotoxicity using a wide range of commercial cell lines including HEK293, HeLa, PC12, and SH-SY5Y.¹⁴ Here, using acute mouse brain slices, we

focused on the cerebral cortex, the suprachiasmatic nucleus (SCN), and anterior hypothalamus (AH). The cerebral cortex is a brain region that exhibits a large degree of neurodegeneration in AD.^{18–21} Conversely, the SCN, the locus of primary circadian clock in mammals,^{22–24} is thought to be relatively resilient to AD, although disruptions in sleep and other circadian rhythms are increasingly acknowledged as early symptoms of AD.^{25–27} The SCN is surrounded by the AH, of which little is known regarding its neurodegenerative vulnerability. Mouse brain slices containing cortex and SCN/AH region were isolated from healthy mice and incubated with either KV11 or G6W peptides (~300 or 400 μ M, respectively; see also Figure S1). After a 4-h incubation, the media surrounding the tissue slices was removed and stored, and the slices were perfused with PI. Slices were then fixed, sectioned, and coverslipped with mounting medium containing DAPI. Cell viability within each brain slice (i.e., tissue viability) was assessed by quantifying DAPI and PI staining using fluorescence imaging.

Overall, as seen in Figure 1, it is clear that KV11 and G6W affected cell viability in all three brain regions. Focusing within the individual brain regions, 2-way ANOVA determined that G6W significantly decreased the percentage of healthy cells in all three brain regions compared to controls ($p < .05$; see Table S3). G6W also significantly decreased the number of healthy cells in the SCN and AH compared to KV11 exposed tissue ($p < .05$). KV11 decreased the percentage of healthy cells in the cortex compared to control conditions, but this did not

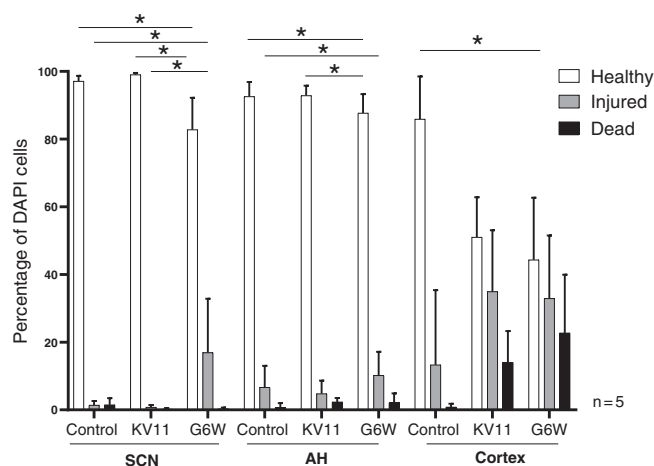


FIGURE 1 Tissue viability assessment under different experimental conditions. Histogram bars indicate the percentage of DAPI-stained cells with different amounts of PI staining. High-intensity PI staining indicates dead cells, moderate PI staining indicates injured cells, and low to no PI staining indicates healthy cells. ($*p < .05$) The error bars represent the standard error mean

reach statistical significance ($p = .093$). G6W increased the number of injured cells in the SCN compared to control conditions and compared to KV11 ($p < .05$). Finally, G6W significantly increased the number of injured cells in the AH compared to the controls ($p < .05$), while the increase in injured cells in the AH compared to KV11 did not quite reach statistical significance ($p = .06$). Taken together, the results indicate that G6W is more toxic than KV11 at least in the SCN and AH, while the toxic effects of KV11 and G6W do not differ significantly between each other in the cortex. The results showing that the SCN, which is considered to be a resilient and robust structure within the brain,²⁸ is affected by amyloids in a manner similar to the cortex are somewhat surprising. Although there was no significant increase in SCN cell death at this time point, it is possible, for example, that toxic peptides are disrupting neuropeptide signaling pathways responsible for SCN neuronal health and synchronization.^{29–31} The data also show that the AH exhibits similar vulnerability to amyloid peptides as the SCN. Few comparisons have been made between these adjacent areas, but cell culture studies have shown that SCN-derived cells exhibit greater excitotoxic resiliency compared to hypothalamus-derived cells.³² These distinct results point to the importance of using intact tissues rather than cell cultures when investigating toxic susceptibility.

An important outcome of these experiments is their demonstration of cellular vulnerability to peptide toxicity during early stages of exposure (i.e., the first 4 h) in all three brain regions. As discussed below, the mechanisms of toxicity are not known. Implicated proteinaceous agents of neurodegenerative disease, such as A β and neurofibrillary tangles of paired tau filaments, are known to accumulate within and around cortex neurons.³³ Cortical neurons may exhibit properties that makes them more vulnerable to degradation and amyloid deposition. For example, differences in firing properties of different neuronal populations within layer II of the entorhinal cortex may contribute to susceptibility to neurodegeneration.³⁴ In future studies, it will be important to extend the duration of amyloid peptide exposure to determine if regional differences in toxic susceptibility become more apparent.

2.2 | IMS-MS reveals that G6W can form large, structurally complex oligomers

The representative mass spectra of KV11 and G6W under the same experimental conditions (20 μ M in 20 mM ammonium acetate pH 7) are shown in Figure 2a,b. Both peptides populate high-order oligomers annotated by nominal n/z where n is oligomer size and z is charge.

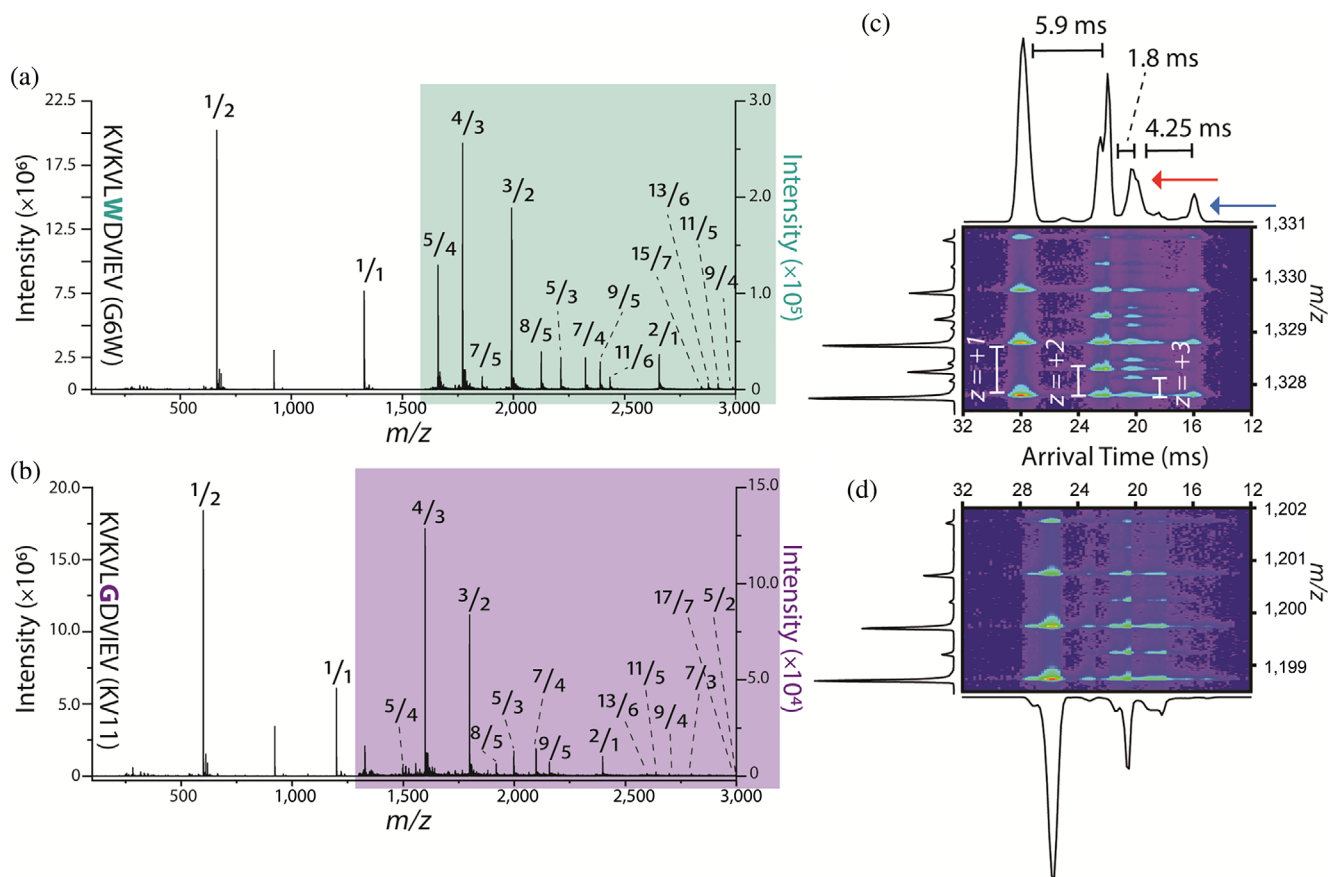


FIGURE 2 Representative mass spectra of (a) G6W and (b) KV11. Each mass spectral peak is labeled by its nominal oligomer-to-charge ratio (n/z). Note that the intensity in the colored regions of each mass spectra is adjusted to reveal less abundant oligomeric species. The 2D plots for $n/z = 1/1$ are shown for both (c) G6W and (d) KV11, where the isotopic spacings can clearly be seen for the features within the ATDs. For G6W, notably, species mentioned in the text are marked with arrows. The data were collected using helium buffer gas

Both mass spectra show intense peaks at $n/z = 3/2$ of which IMS-MS data revealed the presence of trimers ($z = +2$) and hexamers ($z = +4$). The oligomers are unambiguously assigned based on the detected isotopic spacings of $\Delta m/z = 0.5$ and 0.25 , respectively (Figure S2).

Although at first glance, there are slight differences between the mass spectra of G6W and KV11 (e.g., the decapentamer species formed by G6W is not observed in KV11), the major difference between the two peptides can be observed in the arrival time distribution (ATD) of the nominal $n/z = 1/1$ species. The 2D plot (m/z vs. drift time) of G6W (Figure 2c) shows a feature with an arrival time of ~ 20.30 ms (red arrow), which has a distinct pattern of isotopic spacing not seen within the KV11 2D plot (Figure 2d). Within this spacing, one of the patterns indicates that there was a trimer with $z = +3$. The other isotopic spacing pattern suggests that there may also be a dimeric species with $z = +2$ within this feature. However, if this feature were a dimer, then it would have a collisional cross-section (CCS, σ) in helium of 402 \AA^2 which is inconsistent with the $\sigma_{\text{exp,He}}$ values of other

known dimeric species (Table S4). Post-ion-mobility dissociation, a phenomenon we have described in recent work,^{35,36} in which weakly-bound oligomeric species traverse the drift-cell successfully but dissociate before reaching the mass analyzer, may explain the ambiguity we are seeing within the isotopic spacing of this feature.

Additionally, there is a major feature within G6W at 16 ms (blue arrow) that is unique to this peptide. Due to the ambiguity present within the 2D plot, we could not rely solely on isotopic spacing to determine the oligomer size of this feature and therefore needed to incorporate additional data. As G6W oligomerizes to form higher-ordered oligomers, the spacing between the features decreases. For example, between $n/z = 1/1$ and $2/2$, there is a difference of 5.9 ms, while from $2/2$ to $3/3$ there is a difference of 1.8 ms (using helium as the buffer gas). The drift time difference between $3/3$ and the shortest arrival time feature at 16 ms is 4.25 ms. As the oligomers grow in size, the contribution of a monomeric unit to the total oligomer cross-section gets smaller.^{16,37,38} This led us to conclude that the species with the shortest arrival time

feature must not be a tetramer. By comparing the $\sigma_{\text{exp,He}}$ values of potential species that the shortest arrival time feature can represent (Table S5), the oligomer must be a

very large oligomer ($n > 6$). We will further discuss the assignment of this oligomer in the next sections in light of the X-ray crystallography and IMS-MS data on

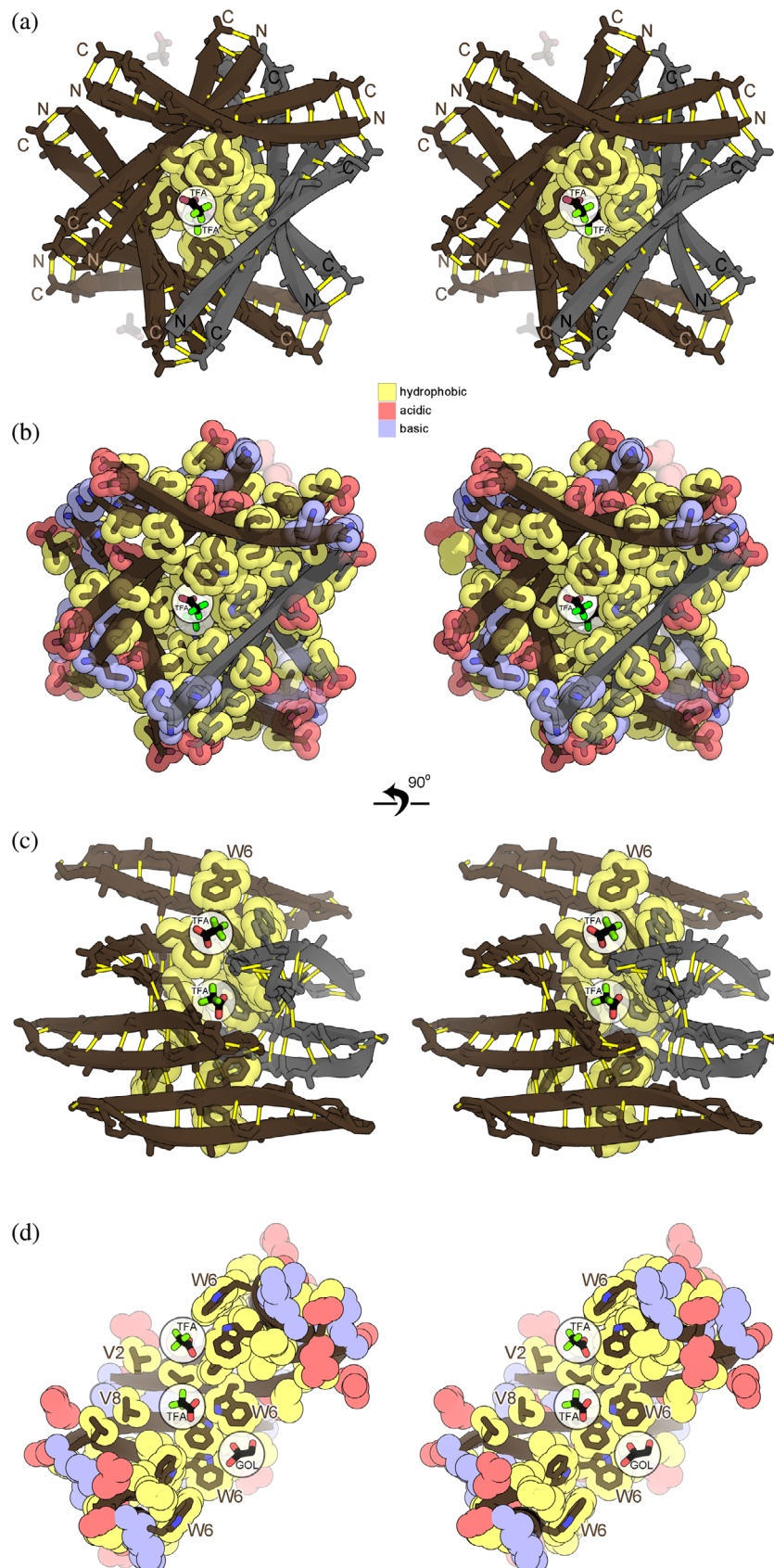


FIGURE 3 The G6W dodecamer crystal structure viewed (a, b) parallel and (c, d) perpendicular to the pseudo 6_4 symmetry axis. Two highly twisted, antiparallel sheets (brown and gray) meet side-by-side at an interface composed of hydrophobic side chains including Trp6 residues, highlighted by van der Waals spheres in panels a and c. Backbone hydrogen bonds are highlighted by yellow lines. Shape complementary between sheets is poor, leaving voids filled by trifluoroacetic acid (TFA) and glycerol (GOL) highlighted by white circles. (b) A space-filling model reveals a charged outside surface (pink and blue spheres) and (d) a cutaway view reveals a hydrophobic core (yellow spheres) with pockets for TFA and GOL binding

interactions of G6W with DDM detergent. Taking all these points into consideration, our IMS-MS data indicated that G6W oligomers are structurally more complex than KV11. G6W can populate two types of oligomers: those that have similar oligomer sizes (not necessarily the same structures) to KV11 (as shown in the analysis of $n/z = 3/2$ species; Figure S2) and those that are distinct from KV11 (as seen in the ATDs of $n/z = 1/1$; Figure 2).

2.3 | G6W assembles into a dodecameric asymmetrical autonomous unit

We used X-ray crystallography to investigate the relationship between the toxicity and the structure of G6W oligomers. Single-crystal diffraction data of both G6W and G6W-Br5 where the fifth residue (Leu) was replaced by L-(2-bromoallyl)-glycine were collected (Table S6). Measurement of anomalous scattering from bromine in G6W-Br5 crystals (Figure S3) allowed us to calculate phases by multiwavelength anomalous dispersion methods. The quality of the electron density map was sufficient to build a full atomic model (Figure S4), and this model proved accurate enough to produce a correct molecular replacement solution for the G6W crystal. We note that G6W-Br5 displayed similar oligomeric structures to G6W, as shown by IMS-MS data in Figure S5. The presence of heavy atoms (Br) allows a more accurate structural refinement.

The crystal structure of G6W reveals a dodecameric assembly distinct from amyloid fibrils. It consists of a pair of β -sheets twisted around a common axis, creating a double helix with approximate 6_422 symmetry (Figure 3a–c). The core of the oligomer prominently features 12 tryptophan side chains, which stack and stabilize the dodecamer through hydrophobic contacts with valine side chains of neighboring β -strands (Figure 3a,c,d and Figure S6). Specifically, each Trp6 sidechain contacts two other Trp6 side chains and Val4 from the opposite β -sheet (Figure S6b). Additionally, the side chain of Val2 abuts Val8 from the opposite β -sheet (Figure S6b). Charged side chains are notably restricted to the outer surface of the oligomer (Figure 3b,d) and are balanced in charge (2 positive and 2 negative per chain).

The G6W structure exhibits four important distinctions from amyloid fibrils. The β -sheets are composed of antiparallel, rather than parallel strands as seen in most amyloid fibril structures. A survey of amyloid fibril literature reveals antiparallel sheet assemblies in only 2 out of ~ 80 fibril structures determined.³⁹ Moreover, the twist of the sheet is much greater in G6W than in amyloid fibrils. On average, β -sheets in G6W twist 30° per β -strand (Figure 3a). In contrast, most amyloid fibrils twist $<2^\circ$

per strand. Then, the β -sheets in G6W crystals are discontinuous; a complete break in hydrogen bonding occurs between β -strands every 50.6 Å along with the sheet (12 strands), separating adjacent oligomers (Figure S7). Such a complete break between adjacent β -strands is unprecedented among amyloid fibril crystal structures and supports the hypothesis that our structure is representative of an oligomer rather than a fibril. Lastly, and most significantly, the fit between mated sheets has poor shape complementarity, creating pockets for ligand binding. The β -sheets in G6W are mated side-by-side through contacts between side chains as is a characteristic of amyloid fibrils; however, the packing is not as tight-fitting as most amyloid steric zippers (Figure S6c).⁴⁰ Indeed, gaps between sheets are filled with trifluoroacetate (TFA) molecules and glycerol (Figure 3).

Such voids in an otherwise stable oligomeric assembly create the potential for biological activity. If the TFA molecules are removed from the structure, a deep and narrow channel becomes evident. It is roughly the size and shape to bind lipids such as palmitic acid (Figure S8), or smaller metabolites. The G6W dodecamer shows a remote structural similarity to lipid transfer proteins (e.g., phosphatidylinositol transfer protein; PITP) and fatty acid binding proteins (FABP). The G6W is made of six pairs of anti-parallel β -strand dimers. PITP binding site (PDB ID 1T27)⁴¹ is formed by the concave surface of an eight-stranded antiparallel β -sheet and two helices. The FABP (PDB ID 1HMR)⁴² consists of 10 antiparallel β -strands and two short helices. The G6W dodecamer has a single nonpolar channel for binding of one acyl tail while PITP and FABP have a lipid headgroup binding pocket and hydrophobic channel(s) for fatty acid tail(s). The toxic mechanism may allude to the role of Apolipoprotein E (APOE) in fat metabolism. Notably, the APOE gene variants are the most commonly associated with late-onset AD.⁴³

Conformational flexibility appears to play a role in creating these binding pockets. Notably, symmetry is lacking between TFA binding sites (Figure 3d), suggesting asymmetry is important to form the pockets. Indeed, a perfectly symmetric conformation observed in the derivative G6W-Br5 (Figure S9) reveals no ligand binding. Conversion between symmetric and asymmetric dodecamers seems plausible given the modular construction of the dodecamer. G6W molecules are bonded tightly into antiparallel β -sheets by 12 backbone hydrogen bonds (Figure S10a). These dimer modules join together at different angles through different numbers of hydrogen bonds (Figure S10c,d). We imagine that small adjustments to these joints, like those demonstrated here between G6W and G6W-Br5, might aid in binding a ligand through an induced-fit mechanism. Imperfect or

mismatched symmetry has been noted as a characteristic of dynamic assemblies such as F_1F_0 ATP synthase.⁴⁴

The presence of an interior channel and flexibility in the dodecameric assembly of G6W molecules distinguish it from the structures of other amyloid oligomers. For example, multiple structures of the parent KV11¹⁴ sequence have been determined, but no variation in the cylindrin architecture was observed and the interior was inaccessible to solvent. Structures of a more distant relative, a segment of superoxide dismutase segment, called “corkscrew”^{5,45} show variation in twist, but exhibited surface grooves rather than an interior channel. All these amyloid oligomers share a robust assembly of antiparallel pairs of β -strands (Figure S11). The dimer modules are held together by full backbone hydrogen bonding and hydrophobic forces between side chains. However, the fit between dimer units varies. The fit between dimers is tight in cylindrin, but poor in G6W, creating voids for ligand binding. This variation in architecture could account for the different patterns of toxic vulnerability incurred by KV11 and G6W.

Our discovery of a potential lipid-binding site and mechanism for ligand binding led us to speculate that G6W might exert its toxicity by binding and damaging the integrity of cell membranes. However, liposome dye-release experiments show that G6W does not induce membrane disruption (Figures S12 and S13). KV11 also does not induce membrane leakage, but expectations for such activity seem lower for KV11 given its lack of obvious lipid-binding pockets.¹⁴ We speculate that the oligomers can extract lipids from the membrane, but are unable to create a pore/channel sufficiently large to leak dye. With that in mind, we tested the hypothesis by studying the assembly of G6W with a membrane mimetic, MS-compatible detergent.

2.4 | G6W dodecamer can be identified with IMS-MS

While G6W does not induce toxicity via causing membrane leakage, here we show that interactions between G6W and membrane mimetics, such as n-Dodecyl- β -D-maltoside (DDM), can affect the self-assembly and stability of G6W oligomers and give rise to very interesting observations. DDM is a nonionic detergent that forms micelles that mimic the cellular membrane and is used frequently in mass spectral analysis of intact membrane-protein complexes.⁴⁶ Additionally, we have previously shown that DDM can be used to explain the differences in toxicity of a set of phenol soluble modulins peptides (PSM α 3).³⁵

The mass spectrum of 15 μ M G6W with 200 μ M DDM in 20 mM ammonium acetate shows that multiple G6W-DDM complexes were formed (Figure S14 and Table S7). Interestingly, some high-ordered G6W oligomers, such as the tetramer, were observed to be in complex with DDM molecules. This was not observed in our early study of PSM α 3 where the complexes consist of only one and at most two PSM α 3.³⁵ A detailed discussion of the G6W-DDM complexes can be found within the Supporting Information.

We note that in the presence of DDM, the ATD of G6W's $n/z = 1/1$ populates features that are otherwise absent or unresolved in the same ATD obtained in the absence of DDM (Figure 4a). There are no G6W-DDM complexes that would have $m/z = 1,327$, so these species must be oligomers of purely G6W (but initially) stabilized or promoted by DDM. The interactions between G6W oligomers and the DDM molecules would slow down the oligomerization of G6W, thus leaving a higher population of more intermediary species such as tetramers and hexamers. Because the interactions are generally weak, the DDM molecules are dissociated before and during IMS measurements. Furthermore, the experimental CCS values of DDM-bound complexes and the new features in the ATD with nominal $n/z = 1/1$ allow for an extrapolation and determination of CCS values of the G6W tetramer and hexamer that are otherwise not observed in the ATD of $m/z = 1,327$.

The presence of these novel features (i.e., oligomers larger than trimer in the ATD of nominal $n/z = 1/1$) can be used to better assign the shortest arrival time feature (blue arrow in Figures 2c and 4a). As noted previously, the arrival time of this feature suggested that this species may be an oligomer with $n > 6$. Initial assignments within the ATD are similar to those in helium shown in Figure 2c. However, now that more features are present within the ATD between the trimer ($n/z = 3/3$) and shortest arrival time feature, there is more information to better assign these large oligomers. The features left of the trimer are assigned as a tetramer (purple arrow), a hexamer (green arrow), and a feature that can contain either an octamer or larger oligomer (blue arrow), respectively. A detailed justification of these assignments can be found within the Supporting Information.

Comparisons of experimental CCS_{He} of potential oligomers for the shortest drift time feature (blue arrow, Figure 2c) and theoretical CCS_{He} are shown in Figure 4b. The theoretical CCS from the X-ray structure (Figure S15) were obtained in helium using the trajectory method.^{47,48} Note that we chose to do the comparison using the helium data because the Mobcal program has the most reliable parameters in helium but not nitrogen.^{47,48} We

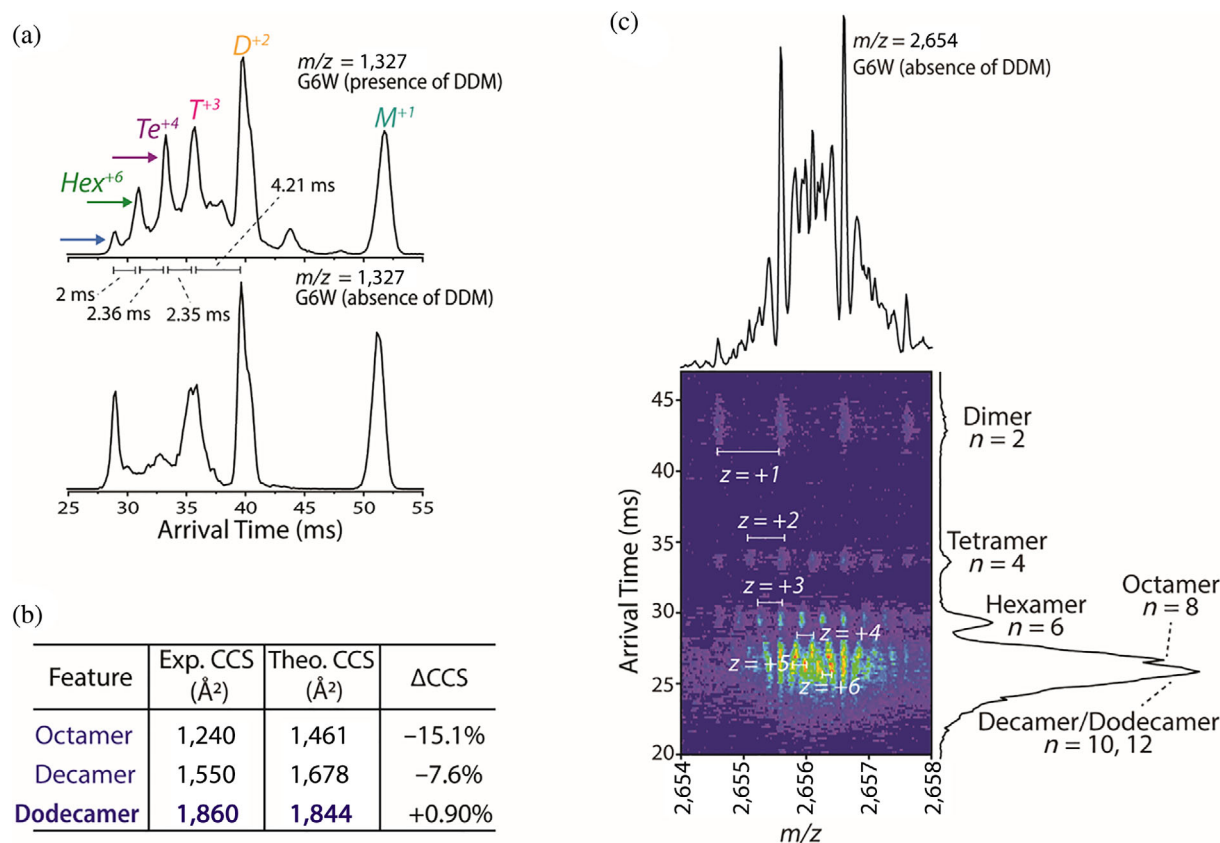


FIGURE 4 (a) Representative ATDs of G6W $n/z = 1/1$ ($m/z = 1,327$) in the presence of DDM (top) and absence of DDM (bottom) in nitrogen buffer gas. The shortest arrival time feature (blue arrow) is tentatively assigned as an octamer, decamer, or dodecamer. (M = monomer, D = dimer, T = trimer, Te = tetramer, Hex = hexamer). (b) Possible oligomeric assignments of the shortest arrival time feature (blue arrow) in both Figure 2c and 4a and comparisons of $\sigma_{\text{exp,He}}$ and $\sigma_{\text{theo,He}}$ of the “double-helix” X-ray structures. Note that these CCS experimental values were obtained in helium in the absence of DDM. (c) 2D plot of G6W in the absence of DDM at $m/z = 2,654$. Each feature within the ATD is assigned according to isotopic spacing detailed by the 2D plot. Note that data shown is collected using helium as the drift gas

found that there was an excellent agreement between the experimental and theoretical CCS of the G6W dodecamer (<1% difference, Figure 4b). Collectively, this evidence points towards the shortest arrival time feature (blue arrow) in both Figures 2c and 4a of being a dodecamer, which agrees with the X-ray model of the G6W oligomer.

To further support this assignment, we searched for similar oligomer distributions from mass spectral peaks at higher m/z (Figure 4c). Our reasoning is that an oligomeric species, if existing in solution and ionized by ESI, will populate multiple charge states. Low-charge state species will have more resolved isotope spacing patterns, allowing us to better identify the existence of such oligomers. Within Figure 4c, we see isotopic spacings that support (1) the existence of octamer, decamer, and dodecamer and (2) the shortest arrival time feature of $m/z = 2,654$ (nominal $n/z = 2/1$) being of a dodecamer. Since we can clearly see such large oligomers in the ATD of other mass spectral peaks, the assignment of the

feature labeled with the blue arrow in both Figures 2c and 4a as a dodecamer is not of pure speculation. This also strengthens our claim that oligomers larger than a decamer are difficult to resolve.

2.5 | Identifying molecules released from SCN/AH tissues may indicate neurochemical pathways that G6W acts upon

To further probe how the G6W oligomers may generate amyloid-disease, LC-IMS-MS was used to identify differences in the chemicals released from SCN/AH-containing brain slices incubated with G6W. In one study performed by Sweedler and co-workers,⁴⁹ rat SCN extracellular samples were collected by placing solid-phase extraction beads on the SCN slice. The beads were then prepared to be analyzed via mass spectrometry to identify

neuropeptide release. Overall, the detection of peptides in releasates is challenging due to their very low concentration. In our study, we chose to sample the peptide contents released from the acute brain slices. A curated library containing the exact mass of mouse neuropeptides (obtained from the previous literature^{50,51}) were used to identify neuropeptide species in the SCN/AH-releasate. Putative neuropeptides significantly up-regulated in the presence of G6W are listed in Table S8 and Figure S16.

Peptides, such as tubulin polymerization-promoting proteins (TPPP) family member 3, were also found upregulated in the G6W SCN + AH releasate. The expression of TPPPs is increased in cortical amyloid plaques of AD patients.⁵² Interestingly, eliminating TPPP expression in mutant mice has been found to affect the circadian timing system.⁵³ Disturbance in circadian rhythms is a common symptom of AD, and could be linked to altered regulation of proteins, such as TPPP. Additional up-regulated peptides include glyceraldehyde-3-phosphate dehydrogenase (GAPDH) and Secretogranin II, both of which have been investigated in the context of AD. Studies have shown that GAPDH can interact with neurodegenerative disease-associated agents,⁵⁴ such as the A β protein precursor,⁵⁵ but its activity is significantly inhibited in AD brains.⁵⁶ Secretogranin II may serve as a potential marker for degradation of neuronal synapses in AD.⁵⁷ Future studies focused on these peptides may generate novel insights into AD processes and potential therapeutics.

3 | CONCLUSION

In summary, our study presents a new model of an amyloid oligomer. X-ray crystallography reveals that the 11-residue peptide G6W (KVKVLWDVIEV) forms large oligomers (dodecamer) composed of 30° twisted antiparallel β -sheets with binding sites that can capture fatty acids or lipids. This is the most structurally complex and unique model of toxic amyloid oligomers reported to date. The differences in oligomer assembly and associated toxicity were investigated by IMS-MS and tissue viability assays. We demonstrated that KV11 and G6W generate distinct levels of cellular damage across regions of the mouse brain that are consistent with AD pathology. More importantly, our work demonstrates that toxic amyloid oligomers can adopt distinct structures, and the structural evolution from one to another can be a result of a single mutation. A mutation targeting one form of toxic amyloids may unexpectedly introduce a new form that is more toxic.

Additionally, we show that interactions between G6W and DDM, a cellular membrane mimetic, lead to an

increased abundance of small G6W oligomers that allowed us to more unambiguously determine the sizes of G6W oligomers formed in the absence of DDM. Finally, we assessed functional changes induced by the amyloid model in the mouse SCN/AH by probing the release of various neuropeptides. While G6W is not an endogenous peptide, it shares a high sequence compatibility with the amyloidogenic cores of A β (i.e., A β ₁₆₋₂₂; KLVFFAE)⁵⁸⁻⁶⁰ and of tau (i.e., PHF6; VQIVYK),^{61,62} which contain aromatic residues known to be crucial for fibril formation and toxicity. Amyloidogenic fragments can exist in vivo as the result of peptidase activities. Collectively, the cytotoxicity of G6W resembles the amyloid effects in AD brains. Its dodecameric structure provides a new model of toxic amyloid oligomers with a novel mechanism to bind fatty acids or lipids.

4 | MATERIALS AND METHODS

All chemicals used in this study were of reagent grade and used without further purification. For IMS-MS and biological experiments, KV11 and G6W were purchased from Genscript (Piscataway, NJ) at >98% purity with TFA removal. IMS-MS data of KV11 and G6W oligomers with and without DDM (Sigma) were acquired by direct infusion of the samples into an Agilent 6560 IM-QTOF mass spectrometer (Santa Clara, CA) in a multi-field experiment with either helium or nitrogen as the drift gas. LC-IMS-MS experiments used an Agilent 1260 Infinity HPLC coupled to an Agilent 6560 IM-QTOF with nitrogen as the drift gas. Instrument parameters and settings can be found in Table S1. LC-IMS-MS data were further processed with Agilent Mass Profiler Professional for molecular feature extraction and neuropeptide identification.

Additional G6W and G6W-Br5 for X-ray crystallography trials were purchased from LifeTein (Somerset, NJ). The peptide sequences are shown in Table S2. Diffraction data of G6W and G6W-Br5 derivatives were obtained at beamline 24-ID-C of the Advanced Photon Source located at Argonne National Laboratory. Liposomes consisting of 100% L- α -phosphatidylcholine (PC) and 90% PC and 10% of either L- α -phosphatidic acid sodium salt (PA) or 1,2-dioleoyl-3-trimethylammonium-propane, chloride salt was prepared, and fluorescence of liposome dye release was measured with a Cary Eclipse Fluorescence Spectrophotometer. A Malvern Zetasizer Nano ZS instrument was used for dynamic light scattering experiments.

Adult male C57BL/6 mice (Envigo; Indianapolis, IN) were housed under 12:12 light:dark cycles with food and water provided ad libitum. Brain slices containing either the SCN and the surrounding AH (two regions within

the same brain slices) or the cortex were incubated in an interface brain slice chamber under static conditions either with Earl's Balanced Salt Solution (EBSS) or with EBSS containing KV11 or G6W peptides for 4 h. The media surrounding the slices was collected and stored for later analysis. The brain slices were maintained further for perfusion with PI, then fixed and sectioned for subsequent histological analysis. Fluorescent images of sectioned tissue were obtained with a Leica DM6000B microscope and analyzed with ImageJ software. Additional information regarding materials, methods, concentrations, animals, and protocols can be found in the Supporting Information.

ACKNOWLEDGMENTS

We thank Duilio Cascio, Michael Collazo, and Génesis Falcón at the UCLA-DOE Crystallization Core Facility for their help in setting up the crystallization trials.

CONFLICT OF INTEREST

There is no conflict of interest to declare.

AUTHOR CONTRIBUTIONS

Amber L. H. Gray: Data curation (equal); formal analysis (lead); investigation (lead); writing – original draft (lead); writing – review and editing (equal). **Michael R. Sawaya:** Data curation (equal); formal analysis (lead); investigation (lead); methodology (equal); project administration (supporting); validation (equal); writing – original draft (equal); writing – review and editing (supporting). **Debalina Acharyya:** Data curation (supporting); formal analysis (supporting); investigation (supporting); methodology (supporting). **Jinchao Lou:** Formal analysis (supporting); investigation (supporting); methodology (supporting). **Emery Edington:** Investigation (supporting). **Michael D. Best:** Methodology (supporting); project administration (supporting); supervision (supporting); writing – review and editing (supporting). **Rebecca A. Prosser:** Conceptualization (equal); formal analysis (equal); methodology (equal); project administration (equal); resources (equal); supervision (supporting); writing – original draft (equal); writing – review and editing (equal). **David S. Eisenberg:** Conceptualization (equal); funding acquisition (supporting); methodology (supporting); project administration (equal); resources (supporting); supervision (equal); writing – review and editing (supporting). **Thanh D. Do:** Conceptualization (lead); formal analysis (supporting); funding acquisition (lead); investigation (supporting); methodology (equal); project administration (lead); resources (lead); supervision (lead); validation (equal); writing – original draft (lead); writing – review and editing (lead).

ORCID

Thanh D. Do  <https://orcid.org/0000-0002-1978-4365>

REFERENCES

- Haass C, Selkoe DJ. Soluble protein oligomers in neurodegeneration: Lessons from the Alzheimer's amyloid β -peptide. *Nat Rev Mol Cell Biol.* 2007;8:101–112.
- Kayed R, Lasagna-Reeves CA. Molecular mechanisms of amyloid oligomers toxicity. *J Alzheimers Dis.* 2013;33:S67–S78.
- Kim YE, Hosp F, Frottin F, et al. Soluble oligomers of PolyQ-expanded huntingtin target a multiplicity of key cellular factors. *Mol Cell.* 2016;63:951–964.
- Bengoa-Vergniory N, Roberts RF, Wade-Martins R, Alegre-Abarrategui J. Alpha-synuclein oligomers: A new hope. *Acta Neuropathol.* 2017;134:819–838.
- Sangwan S, Zhao A, Adams KL, et al. Atomic structure of a toxic, oligomeric segment of SOD1 linked to amyotrophic lateral sclerosis (ALS). *Proc Natl Acad Sci USA.* 2017;114:8770–8775.
- Ghiso J, Frangione B. Amyloidosis and Alzheimer's disease. *Adv Drug Deliv Rev.* 2002;54:1539–1551.
- Fu H, Hardy J, Duff KE. Selective vulnerability in neurodegenerative diseases. *Nat Neurosci.* 2018;21:1350–1358.
- Boillée S, Vande Velde C, Cleveland DW. ALS: A disease of motor neurons and their nonneuronal neighbors. *Neuron.* 2006;52:39–59.
- Brichta L, Greengard P. Molecular determinants of selective dopaminergic vulnerability in Parkinson's disease: An update. *Front Neuroanat.* 2014;8:152.
- Roselli F, Caroni P. From intrinsic firing properties to selective neuronal vulnerability in neurodegenerative diseases. *Neuron.* 2015;85:901–910.
- Saxena S, Caroni P. Selective neuronal vulnerability in neurodegenerative diseases: From stressor thresholds to degeneration. *Neuron.* 2011;71:35–48.
- Österlund N, Moons R, Ilag LL, Sobott F, Gräslund A. Native ion mobility-mass spectrometry reveals the formation of β -barrel shaped amyloid- β hexamers in a membrane-mimicking environment. *J Am Chem Soc.* 2019;141:10440–10450.
- Serra-Batiste M, Ninot-Pedrosa M, Bayoumi M, Gairí M, Maglia G, Carulla N. A β 42 assembles into specific β -barrel pore-forming oligomers in membrane-mimicking environments. *Proc Natl Acad Sci USA.* 2016;113:10866–10871.
- Laganowsky A, Liu C, Sawaya MR, et al. Atomic view of a toxic amyloid small oligomer. *Science.* 2012;335:1228–1231.
- Tayeb-Fligelman E, Tabachnikov O, Moshe A, et al. The cytotoxic *Staphylococcus aureus* PSM α 3 reveals a cross- α amyloid-like fibril. *Science.* 2017;355:831–833.
- Do TD, LaPointe NE, Nelson R, et al. Amyloid β -protein C-terminal fragments: Formation of Cylindrins and β -barrels. *J Am Chem Soc.* 2016;138:549–557.
- Laos V, Do TD, Bishop D, et al. Characterizing TDP-43307-319 oligomeric assembly: Mechanistic and structural implications involved in the etiology of amyotrophic lateral sclerosis. *ACS Chem Neurosci.* 2019;10:4112–4123.
- Armstrong RA, Lantos PL, Cairns NJ. The spatial patterns of prion protein deposits in Creutzfeldt-Jakob disease:

- comparison with β -amyloid deposits in Alzheimer's disease. *Neurosci Lett*. 2001;298:53–56.
19. Dickerson BC, Bakkour A, Salat DH, et al. The cortical signature of Alzheimer's disease: Regionally specific cortical thinning relates to symptom severity in very mild to mild AD dementia and is detectable in asymptomatic amyloid-positive individuals. *Cereb Cortex*. 2009;19:497–510.
 20. Dugger BN, Dickson DW. Pathology of neurodegenerative diseases. *Cold Spring Harb Perspect Biol*. 2017;9:a028035.
 21. Giannakopoulos P, Hof PR, Michel J-P, Guimon J, Bouras C. Cerebral cortex pathology in aging and Alzheimer's disease: A quantitative survey of large hospital-based geriatric and psychiatric cohorts. *Brain Res Rev*. 1997;25:217–245.
 22. Buijs RM, Escobar C, Swaab DF. Chapter 15—The circadian system and the balance of the autonomic nervous system. In: Buijs RM, Swaab DF, editors. *Handbook of clinical neurology*. Volume 117. Amsterdam, The Netherlands: Elsevier, 2013; p. 173–191.
 23. Mohawk JA, Green CB, Takahashi JS. Central and peripheral circadian clocks in mammals. *Annu Rev Neurosci*. 2012;35:445–462.
 24. Morin LP. Neuroanatomy of the extended circadian rhythm system. *Exp Neurol*. 2013;243:4–20.
 25. Fernandez F-X, Kaladchibachi S, Negelspach DC. Resilience in the suprachiasmatic nucleus: Implications for aging and Alzheimer's disease. *Exp Gerontol*. 2021;147:111258.
 26. Stopa EG, Volicer L, Kuo-Leblanc V, et al. Pathologic evaluation of the human suprachiasmatic nucleus in severe dementia. *J Neuropathol Exp Neurol*. 1999;58:29–39.
 27. Van Erum J, Van Dam D, De Deyn PP. Sleep and Alzheimer's disease: A pivotal role for the suprachiasmatic nucleus. *Sleep Med Rev*. 2018;40:17–27.
 28. Butler MP, Silver R. Basis of robustness and resilience in the suprachiasmatic nucleus: Individual neurons form nodes in circuits that cycle daily. *J Biol Rhythms*. 2009;24:340–352.
 29. Dardente H, Menet JS, Challet E, Tournier BB, Pévet P, Masson-Pévet M. Daily and circadian expression of neuropeptides in the suprachiasmatic nuclei of nocturnal and diurnal rodents. *Mol Brain Res*. 2004;124:143–151.
 30. Irwin RP, Allen CN. Neuropeptide-mediated calcium signaling in the suprachiasmatic nucleus network. *Eur J Neurosci*. 2010;32:1497–1506.
 31. Mitchell JW, Atkins N, Sweedler JV, Gillette MU. Direct cellular peptidomics of hypothalamic neurons. *Front Neuroendocrinol*. 2011;32:377–386.
 32. Bottum K, Poon E, Haley B, Karmarkar S, Tischkau SA. Suprachiasmatic nucleus neurons display endogenous resistance to excitotoxicity. *Exp Biol Med (Maywood)*. 2010;235:237–246.
 33. Garcia-Marin V, Blazquez-Llorca L, Rodriguez JR, et al. Diminished perisomatic GABAergic terminals on cortical neurons adjacent to amyloid plaques. *Front Neuroanat*. 2009;3:28.
 34. Stranahan AM, Mattson MP. Selective vulnerability of neurons in layer II of the entorhinal cortex during aging and Alzheimer's disease. *Neural Plast*. 2010;2010:108190.
 35. Gray ALH, Antevska A, Oluwatoba DS, Schonfeld GE, Lazar Cantrell KL, Do TD. Cytotoxicity of α -helical, *Staphylococcus aureus* PSM α 3 investigated by post-ion-mobility dissociation mass spectrometry. *Anal Chem*. 2020;92:11802–11808.
 36. Link BA, Sindt AJ, Shimizu LS, Do TD. Selective host-guest chemistry, self-assembly and conformational preferences of m-xylene macrocycles probed by ion-mobility spectrometry mass spectrometry. *Phys Chem Chem Phys*. 2020;22:9290–9300.
 37. Bernstein SL, Dupuis NF, Lazo ND, et al. Amyloid- β protein oligomerization and the importance of tetramers and dodecamers in the aetiology of Alzheimer's disease. *Nat Chem*. 2009;1:326–331.
 38. Bleiholder C, Dupuis NF, Wytenbach T, Bowers MT. Ion mobility-mass spectrometry reveals a conformational conversion from random assembly to β -sheet in amyloid fibril formation. *Nat Chem*. 2011;3:172–177.
 39. Sawaya MR, Hughes MP, Rodriguez JA, Riek R, Eisenberg DS. The expanding amyloid family: Structure, stability, function, and pathogenesis. *Cell*. 2021;184:4857–4873.
 40. Eisenberg DS, Sawaya MR. Structural studies of amyloid proteins at the molecular level. *Annu Rev Biochem*. 2017;86:69–95.
 41. Yoder MD, Thomas LM, Tremblay JM, Oliver RL, Yarbrough LR, Helmkamp GM Jr. Structure of a multifunctional protein. Mammalian phosphatidylinositol transfer protein complexed with phosphatidylcholine. *J Biol Chem*. 2001;276:9246–9252.
 42. Young AC, Scapin G, Kromminga A, Patel SB, Veerkamp JH, Sacchetti JC. Structural studies on human muscle fatty acid binding protein at 1.4 Å resolution: Binding interactions with three C18 fatty acids. *Structure*. 1994;2:523–534.
 43. Liu C-C, Kanekiyo T, Xu H, Bu G. Apolipoprotein E and Alzheimer disease: Risk, mechanisms and therapy. *Nat Rev Neurol*. 2013;9:106–118.
 44. Junge W, Pänke O, Cherepanov DA, Gumbiowski K, Müller M, Engelbrecht S. Inter-subunit rotation and elastic power transmission in F₀F₁-ATPase. *FEBS Lett*. 2001;504:152–160.
 45. Sangwan S, Sawaya MR, Murray KA, Hughes MP, Eisenberg DS. Atomic structures of corkscrew-forming segments of SOD1 reveal varied oligomer conformations. *Protein Sci*. 2018;27:1231–1242.
 46. Laganowsky A, Reading E, Hopper JTS, Robinson CV. Mass spectrometry of intact membrane protein complexes. *Nat Protoc*. 2013;8:639–651.
 47. Mesleh MF, Hunter JM, Shvartsburg AA, Schatz GC, Jarrold MF. Structural information from ion mobility measurements: Effects of the long-range potential. *J Phys Chem*. 1996;100:16082–16086.
 48. Shvartsburg AA, Jarrold MF. An exact hard-spheres scattering model for the mobilities of polyatomic ions. *Chem Phys Lett*. 1996;261:86–91.
 49. Hatcher NG, Atkins N, Annangudi SP, et al. Mass spectrometry-based discovery of circadian peptides. *Proc Natl Acad Sci USA*. 2008;105:12527–12532.
 50. Lee JE, Zamdborg L, Southey BR, et al. Quantitative peptidomics for discovery of circadian-related peptides from the rat suprachiasmatic nucleus. *J Proteome Res*. 2013;12:585–593.
 51. Lee JE, Atkins N Jr, Hatcher NG, et al. Endogenous peptide discovery of the rat circadian clock: A focused study of the suprachiasmatic nucleus by ultrahigh performance tandem mass spectrometry. *Mol Cell Proteomics*. 2010;9:285–297.

52. Drummond E, Nayak S, Faustin A, et al. Proteomic differences in amyloid plaques in rapidly progressive and sporadic Alzheimer's disease. *Acta Neuropathol.* 2017;133:933–954.
53. Barbato E, Darrah R, Kelley TJ. Tubulin polymerization promoting protein affects the circadian timing system in C57Bl/6 mice. *J Circadian Rhythms.* 2021;19:5.
54. Burke JR, Enghild JJ, Martin ME, et al. Huntingtin and DRPLA proteins selectively interact with the enzyme GAPDH. *Nat Med.* 1996;2:347–350.
55. Schulze H, Schuler A, Stüber D, Döbeli H, Langen H, Huber G. Rat brain glyceraldehyde-3-phosphate dehydrogenase interacts with the recombinant cytoplasmic domain of Alzheimer's beta-amyloid precursor protein. *J Neurochem.* 1993;60:1915–1922.
56. Butterfield DA, Hardas SS, Lange ML. Oxidatively modified glyceraldehyde-3-phosphate dehydrogenase (GAPDH) and Alzheimer's disease: Many pathways to neurodegeneration. *J Alzheimers Dis.* 2010;20:369–393.
57. Marksteiner J, Kaufmann WA, Gurka P, Humpel C. Synaptic proteins in Alzheimer's disease. *J Mol Neurosci.* 2002;18:53–63.
58. Boyd-Kimball D, Abdul HM, Reed T, Sultana R, Butterfield DA. Role of phenylalanine 20 in Alzheimer's amyloid, beta-peptide (1–42)-induced oxidative stress and neurotoxicity. *Chem Res Toxicol.* 2004;17:1743–1749.
59. Genji M, Yano Y, Hoshino M, Matsuzaki K. Aromaticity of phenylalanine residues is essential for amyloid formation by Alzheimer's amyloid beta-peptide. *Chem Pharm Bull.* 2017;65:668–673.
60. Cukalevski R, Boland B, Frohm B, Thulin E, Walsh D, Linse S. Role of aromatic side chains in amyloid beta-protein aggregation. *ACS Chem Neurosci.* 2012;3:1008–1016.
61. Ganguly P, Do TD, Larini L, et al. Tau assembly: The dominant role of PHF6 (VQIVYK) in microtubule binding region repeat R3. *J Phys Chem B.* 2015;119:4582–4593.
62. Ait-Bouziad N, Chiki A, Limorenko G, Xiao S, Eliezer D, Lashuel HA. Phosphorylation of the overlooked tyrosine 310 regulates the structure, aggregation, and microtubule- and lipid-binding properties of tau. *J Biol Chem.* 2020;295:7905–7922.

SUPPORTING INFORMATION

Additional supporting information may be found in the online version of the article at the publisher's website.

How to cite this article: Gray ALH, Sawaya MR, Acharyya D, Lou J, Edington EM, Best MD, et al. Atomic view of an amyloid dodecamer exhibiting selective cellular toxic vulnerability in acute brain slices. *Protein Science.* 2022;31:716–27. <https://doi.org/10.1002/pro.4268>